Journal of ELECTRONIC MATERIALS, Vol. 46, No. 4, 2017
DOI: 10.1007/s11664-016-5271-1
© 2017 The Minerals, Metals & Materials Society

CrossMark

Optical and Compositional Properties of SiO*x* Films Deposited by HFCVD: Effect of the Hydrogen Flow

J.A. LUNA LÓPEZ,[1,4] D.E. VÁZQUEZ VALERDI,[1,5] A. BENÍTEZ LARA,[3,6] G. GARCÍA SALGADO,[1,7] A.D. HERNÁNDEZ-DE LA LUZ,[1,8] A. MORALES SÁNCHEZ,[2,9] F.J. FLORES GRACIA,[1,10] and M.A. DOMINGUEZ,[1,11]

1.—IC-CIDS Benemérita Universidad Autónoma de Puebla, Ed. 103 C o D, Col. San Manuel, C.P. 72570 Puebla, Pue., Mexico. 2.—Centro de Investigación en Materiales Avanzados S. C., CIMAV-Unidad Monterrey-PIIT, Apodaca, Nuevo León, Mexico. 3.—Department of Physics and Astronomy, University of Texas at San Antonio, One UTSA Circle, San Antonio, TX 78249. 4.—e-mail: jose.luna@correo.buap.mx. 5.—e-mail: dianeli1@hotmail.com. 6.—e-mail: alfredbl@gmail.com. 7.—e-mail: godgarcia@yahoo.com. 8.—e-mail: joalvada1@hotmail.com. 9.—e-mail: alfredo.morales@cimav.edu.mx. 10.—e-mail: pacofloresgracia@gmail.com. 11.—e-mail: madominguezj@gmail.com

In this work, the effect of hydrogen flow and thermal annealing on the compositional and optical properties of non-stoichiometric silicon oxide (SiO*x*) films with embedded silicon nanocrystals is reported. The SiO_x films are obtained by hot filament chemical vapor deposition technique at three different hydrogen flow levels, namely, 50 sccm, 100 sccm, and 150 sccm. The SiO*x* films are characterized by different techniques. It is found by x-ray photoelectron spectroscopy (XPS) that with increasing hydrogen flow, the SiO*x* films contain higher silicon (Si) concentration. When the hydrogen flow decreases, the absorption edge of the as-grown SiO*x* films, as obtained from the transmittance spectra, shifts from 300 nm to 500 nm, and this opens the possibility of band gap tuning. Increasing the hydrogen flow level in turn means that the SiO*x* films contain higher Si concentration, as confirmed by the XPS profile composition measured in the SiO*x* films. After thermal annealing, the SiO*x* films transmittance spectra showed a further shift of the absorption edge toward larger wavelengths. The Fourier transform infrared (FTIR) spectroscopy reveals film composition changes induced by the hydrogen flow variations. In addition, the FTIR spectra reveal the bands attributed to the hydrogen presence in the as-grown SiO*x* films. The bands become more intense with increasing hydrogen flow, but they rapidly disappear after the thermal annealing. The as-grown SiO*x* films exhibit wide band photoluminescence (PL) spectra with the main components at 688 nm, 750 nm, and 825 nm. The SiO*x* film deposited at 100 sccm hydrogen flow level shows the strongest PL intensity. According to PL results, the thermal annealing of the SiO*x* films generates the PL quenching in all samples due to hydrogen evaporation. The defects such as OH and Si–H groups in the as-grown SiOx films not only modify the optical band gap structure, but they also play the role of passivating non-radiative defects, which enhances the PL emission.

Key words: SiO*x* films, HFCVD, XPS, FTIR, photoluminescence, transmittance, annealing

(Received January 19, 2016; accepted December 29, 2016; published online January 24, 2017)

INTRODUCTION

Non-stoichiometric silicon oxide films (SiO*x*, $x < 2$) have already been intensively studied

because of their technological importance for silicon-based optoelectronic devices. Because SiOx is a combination of stoichiometric oxide (SiO_2), a non-stoichiometric suboxide (SiOx, $x < 2$), and silicon nanocrystals (Si-ncs), it is difficult to determine a simple electron energy band diagram to study its optical and electronic properties. However, through theoretical studies using first principles methods it has been possible to understand some its basic optical and electronic properties.[1,2] In SiOx, the formation of Si-ncs embedded in the matrix is noticeable and it implies optical effects due to quantum confinement, which determines mainly an efficient emission of visible light even at room temperature.[3–6] Further, such structures are highly desirable for the integration of optical signals with electronic data processing circuits in the same chip.[7–10] On the other hand, it has been established that blue and green photoluminescence (PL) observed in SiOx films is related to several emitting centers in the silicon oxide, while the origin of the PL band in the orange-red region is still a topic of investigation by the scientific community.[11–13] SiOx can be prepared by different techniques within which we find silicon ion implantation into the thermal dioxide films,[14] reactive sputtering,[4,15] co-evaporation,[16] low-pressure chemical vapor deposition (LPCVD), hot filament chemical vapor deposition (HFCVD),[17] and plasma enhanced chemical vapor deposition (PECVD).[18] A common feature of all these techniques is that changes in the process parameters allow controlling the silicon (Si) excess in the SiOx films. In order to gain the radiative emission of this material, thermal treatments are generally needed to increase the luminescent properties of the SiOx films because they generate a crystallization, which activates luminescence in the material. Such luminescent mechanisms are greatly influenced by the presence of chemical elements used in the process to obtain the SiOx films. A few techniques can produce Si-ncs in as-grown SiOx films, so we find that one of them is the HFCVD technique, similar as that which produces the nanodiamond and carbon nanotubes.[19–23] In this work, the effects of the hydrogen flow level during the deposition, as well as the effect of the subsequent thermal treatment on the compositional and optical properties of SiOx films obtained by the HFCVD technique, are evaluated. We point out the influence of the hydrogen flow level on the Si excess embedded in the SiOx films. It is important because the optical energy band gap may be increased by deposition parameters variation. Additionally, the generation of some of the radiative defects such as neutral oxygen vacancy (NOV), weak oxygen bond (WOB), and the non-bridging oxygen hole center (NBOHC), in the as-grown films contribute to the PL phenomenon. This fact gives a possibility to design SiOx films with specific structural and optical characteristics just by controlling the hydrogen flow levels and growth temperature; these characteristics can be used, in principle, in the field of optoelectronic devices.

EXPERIMENTAL DEVELOPMENT

The SiOx films were deposited on quartz and n-type silicon (100) substrates with 1–10 Ω-cm resistivity, by the HFCVD technique in a range of temperatures from 870°C to 890°C, using a fused quartz rod as the reactive source. The deposition time was 5 min for the SiOx films. The substrates were cleaned with a metal oxide semiconductor (MOS) standard cleaning process and the native silicon oxide was removed with a hydrofluoric (HF)-Buffer solution. A schematic diagram of the home-made HFCVD-vertical configuration is shown in Fig. 1.

The HFCVD technique consists in dissociating molecular hydrogen in atomic hydrogen by using six tungsten filaments heated at ~2000°C. Once the atomic hydrogen (H) is obtained, it reacts with the quartz source and produces the precursors that are transported to the substrate. Nowadays, the more accepted chemical reactions between the atomic hydrogen and the solid quartz source is the following: $2H^0(g) + SiO_2(s) \rightarrow SiO(g) + H_2O(g)$, where water ($H_2O$) and silicon monoxide (SiO) are the molecular precursors of this reaction. After these precursors are transported to the substrate by the molecular hydrogen flow and diffusion process, a subsequent chemical reaction is carried out, which is as follows: $SiO(g) + H_2O(g) \rightarrow SiO_2(s) + H_2(g)$, it is schematically indicated in Fig. 2.

The SiOx films were deposited taking into account three different hydrogen flow levels, namely, 50 sccm, 100 sccm, and 150 sccm using quartz rods

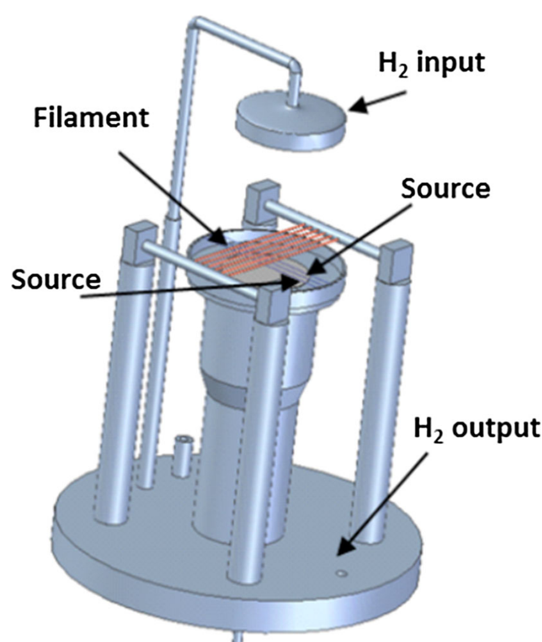

Fig. 1. A schematic diagram of the homemade HFCVD system.

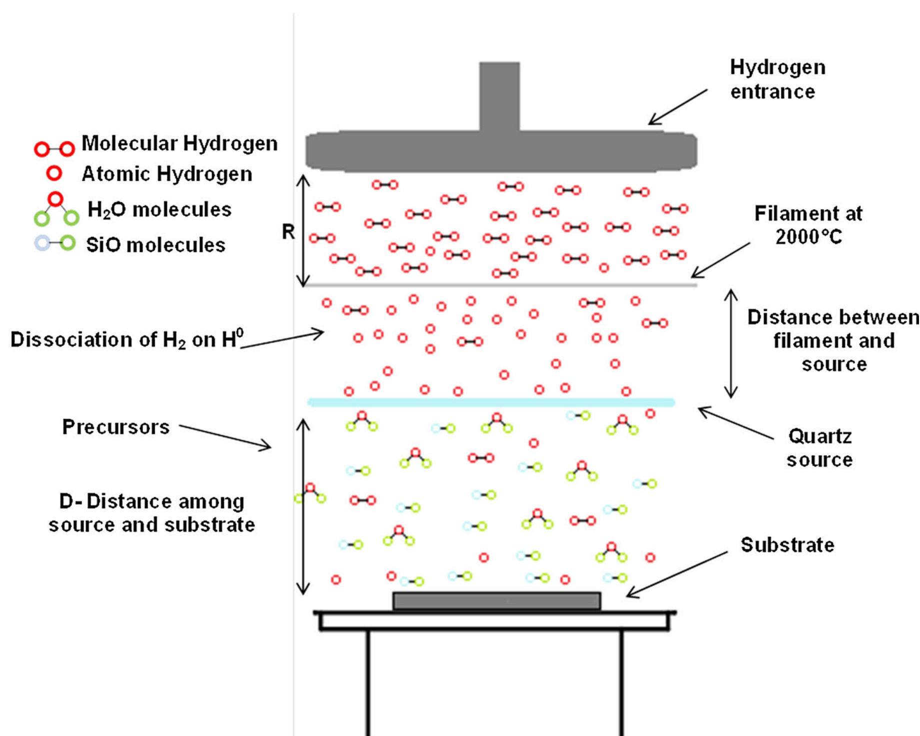

Fig. 2. Schematic stages of the deposit process that give rise to the formation of SiO*x* films.

(5.3 cm length, 2 mm diameter) as source. The growth temperature depends on the source-substrate distance. The filament-source distance and the source-substrate distance, where the latter determines the growth temperature, were fixed at 3 mm and 5 mm, respectively. After deposition, the SiO*x* samples were thermally annealed at 1100°C for 60 min in nitrogen atmosphere. Table I shows the experimental conditions of the samples deposited. The compositional and optical properties of the SiO*x* films were obtained using different spectroscopic techniques. The film thickness was measured using a Dektak 150 profilometer (Veeco Instruments Inc., Plainview, NY, USA); in this case five different scans were done for each sample. X-ray photoelectron spectroscopy (XPS) analysis was carried out using an Escalab250Xi Thermo Scientific spectrometer with a monochromatic Al radiation XR6 and energy of 1486.68 eV. Fourier transform infrared (FTIR) spectroscopy measurements were done using a Bruker system model vector 22 (Bruker Instruments, Bellirica, MA, USA). Transmittance spectra of the SiO*x* films were measured using a UV–Vis–NIR Cary 5000 system (Agilent technologies Inc., Santa Clara, CA, USA). The transmittance signal was collected from 200 nm to 1000 nm with a resolution of 0.5 nm. PL response was measured at room temperature using a Horiba JobinYvon spectrometer model FluroMax 3 (Edison, NJ, USA) with a pulsed xenon source whose detector has a multiplier tube, which is controlled by a computer. The samples were excited using a 250-nm radiation and the PL response was recorded between 380 nm and 1000 nm with a resolution of 1 nm. High resolution scanning electron microscopy measurement was done using a HRSEM Auriga model FE 3916, which operates with a column GENIMI Schottky emission working in the field from 0.1 keV to 30 keV range and achieves a resolution of 1.0 nm @ 15 kV. High resolution transmission electron microscopy (HRTEM) measurement was done using a JEOL system model JEM-2010, which operates at 200 kV.

RESULTS AND DISCUSSION

The thicknesses of the SiO*x* films as a function of the hydrogen flow levels are shown in Fig. 3 through the box statistic charts; the mean, maximum, and minimum values are depicted, where the width of each box denotes the standard deviation of the measurements, and five different scans were done for each sample. According to these results, we take for granted that the hydrogen flow affects the thickness of the SiO*x* films. Figure 3 reveals the thinnest and the most uniform SiO*x* films, which were obtained using a hydrogen flow level at 100 sccm (~1 μm). On average, the film thicknesses were obtained from 1 μm to 8 μm and were continuous-like, as is shown in Fig. 4, which was obtained from SEM micrography. The insets in Fig. 4a and b show a cross section of the SiO*x* films thickness and is reported in another SiO*x* films work.[15–29]

The XPS-Si 2*p* spectra and their evolution in the surface, volume (middle), and SiO*x*/Si interface

Table I. Experimental conditions of the grown SiOx films

Distance filament-source 3 mm	SiOx deposited					
Distance source-substrate 5 mm	As grown			Annealed		
Flow level (sccm)	50	100	150	50	100	150
SiOx samples	A50	B100	C150	A50TT	B100TT	C150TT

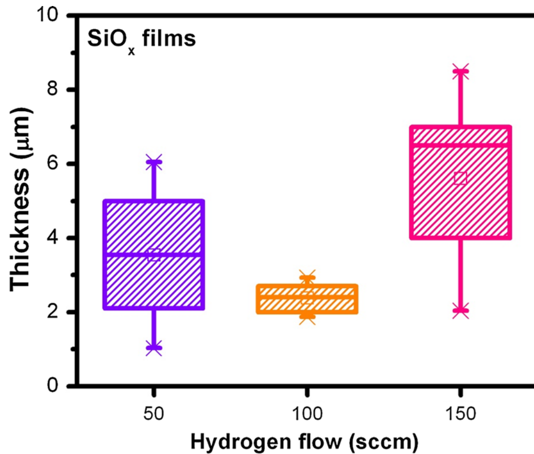

Fig. 3. Variations of the SiOx films thickness as a function of the hydrogen flow level.

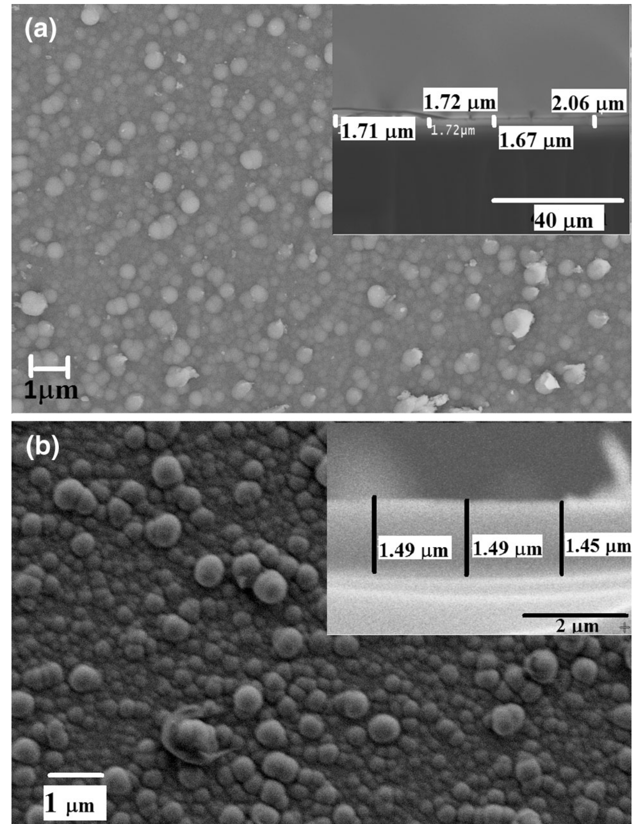

Fig. 4. SEM micrograph of the SiOx films (a) as-grown and (b) annealed. Insets show cross section observed from the films thickness.

(depth) of the SiOx films deposited at 50 sccm, 100 sccm, and 150 sccm hydrogen flow levels for as-grown and after thermal annealing are shown in Fig. 5. This figure exhibits six graphics, the top set correspond to the SiOx film deposited at 50 sccm hydrogen flow level, the middle set at 100, and the bottom set at 150 sccm, denoted Fig. 5a, b, c, d, e, and f, respectively; all graphics consider both the as-grown and annealed conditions. As is well known, when Si is considered a single element, their overlapped binding energies of the core shell levels $2p_{1/2}$, $2p_{3/2}$ both identified as $2p$ have peaks at about 99 eV. Nevertheless, when Si is taken as a compound (e.g. SiO_2) this peak shifts to a bigger binding energy at about 103 eV. On the other hand, it is widely accepted that the Si $2p$ photoelectron peak of SiOx contains five components, one of which corresponds to a non-oxidized state and the remaining four to different oxidation states of Si.[27,28] The four oxidation states, as well as the non-oxidized state, can be modeled as tetrahedral bonds units, in which a central Si atom is bonded to $(4 - n)$ Si atoms and n oxygen atoms ($Si–Si_{4-n}\ O_n$) with n = 0–4. In the SiOx layer, the five oxidation states can be identified by the chemical structures, Si, Si_2O, SiO, Si_2O_3, and SiO_2, which correspond to the oxidation states Si^{0+}, Si^{1+}, Si^{2+}, Si^{3+}, and Si^{4+} respectively, where the sub-oxides correspond to the three states Si^{n+} (n = 1,2,3). In general, these oxidation states contribute to the XPS Si $2p$ spectrum in the SiOx films, and their remarkable presence depends on the at.% concentration of each in the material. Thus, we first have at the top left graphic in Fig. 5a the Si $2p$ spectrum, which considers a SiOx film as grown at 50 sccm hydrogen flow level. This spectrum has two different curves associated with the three regions where the curves ascribed to the deep and middle regions are overlapped and cannot be distinguished clearly. These overlapped curves exhibit a main peak at about 103 eV with a left adjacent shoulder peak at about 100 eV. The inset in this figure shows the deconvolution of the peaks and three different oxidation states or sub-oxides are obtained, while the curve associated with the surface region presents two pronounced peaks

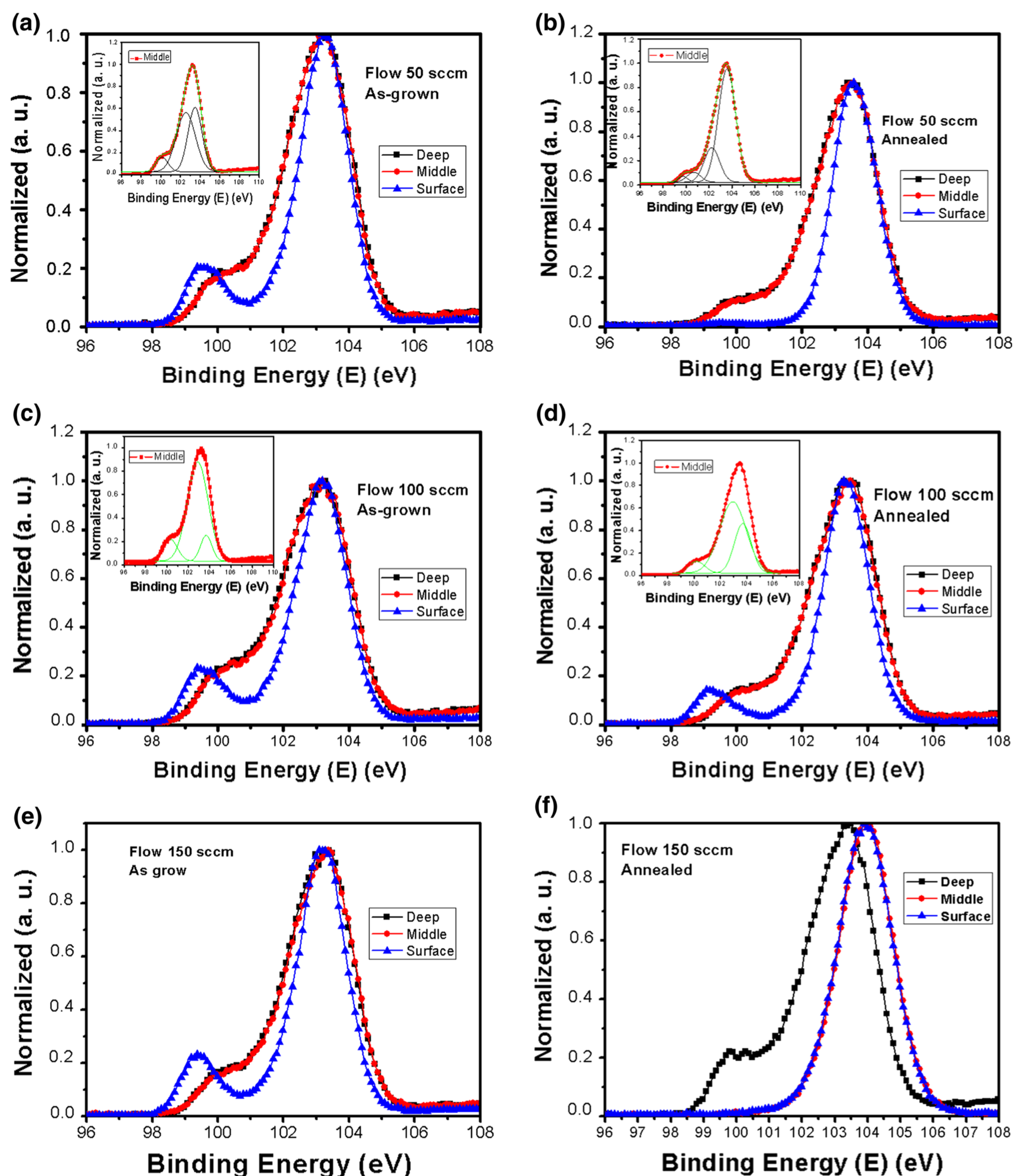

Fig. 5. XPS Si 2*p* spectra of the as-grown and thermally annealed SiO*x* films deposited at 50 sccm [with (a) as grown and (b) annealed], 100 sccm [with (c) as grown and (d) annealed], and 150 sccm [with (e) as grown and (f) annealed] hydrogen flow level. Insets show deconvolution of some XPS spectra.

located at about 99 eV and 103 eV. They are attributed to the oxidation state Si^{0+}(Si) and Si^{4+}(SiO_2), respectively, and any other variation could be attributed to the presence of the suboxides.[25,26] However, for the case of the overlapped curves corresponding to the deep and middle regions the oxidation state Si^{0+}(Si) is not well identified, which means that in these regions the atomic percentage concentration of this state has been reduced so that it tends to disappear. In relation to the Si^{4+}(SiO_2) oxidation state, its at.% concentration is practically unaffected being the corresponding binding energy the same as that of the surface region. In Fig. 5a the inset shows the Si 2*p* peaks, which have been deconvoluted in the different silicon environments in order to clarify the contribution of the Si^{0+}(Si) and Si^{4+}(SiO_2) oxidation states. On the other hand, at the top right graphic, Fig. 5b, the Si 2*p* spectrum corresponds to the SiO*x* film annealed and grown at 50 sccm flow level. As observed, the thermal annealing applied on the SiO*x* films affects mainly the XPS Si 2*p* spectrum

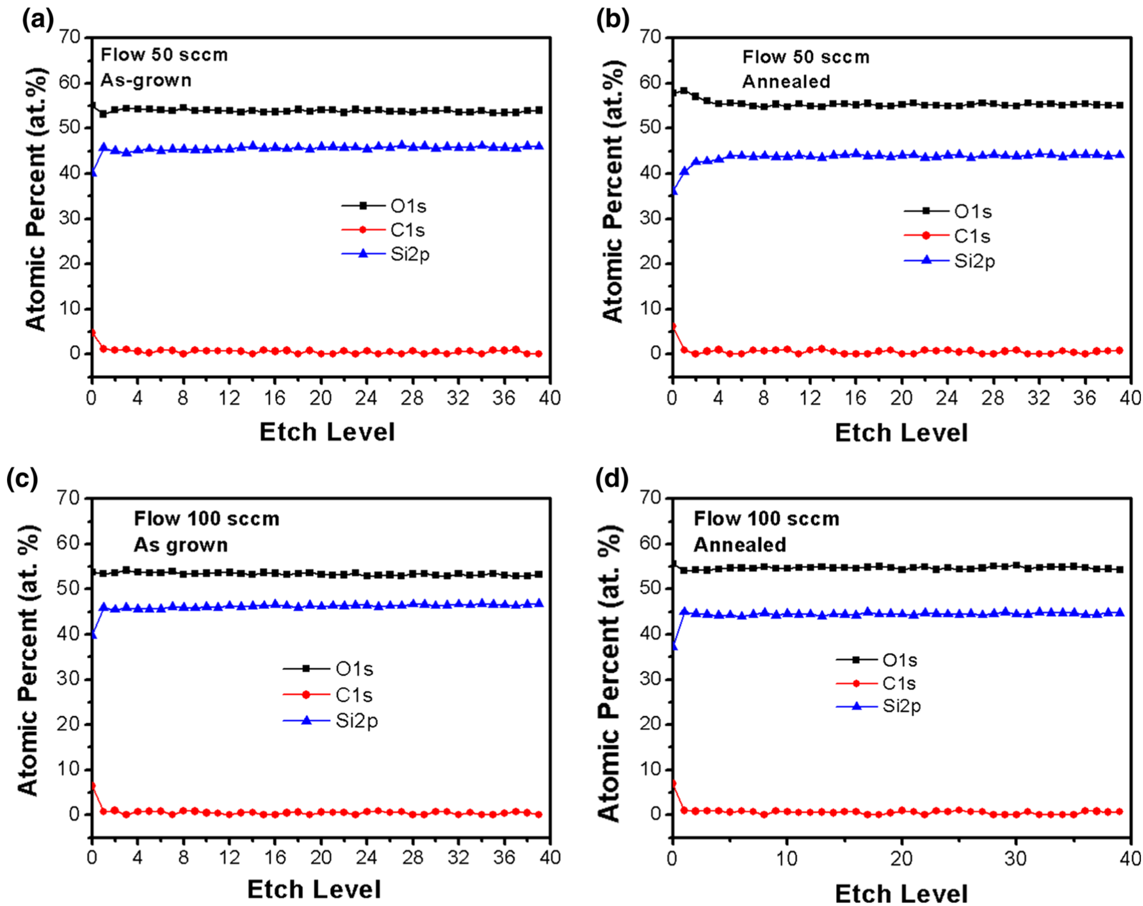

Fig. 6. XPS depth composition profile of the as-grown and thermally annealed SiO*x* films deposited at 50 sccm [with (a) as grown and (b) annealed] 100 sccm [with (c) as grown and (d) annealed] flow levels.

associated with the surface region since the contribution of the Si^{0+}(Si) oxidation state has disappeared, leaving only the contribution of the Si^{4+}(SiO_2) oxidation state whose binding energy is kept the same as the as-grown case. Here the contribution of the oxidation states has been remarkably reduced such that there is a tendency to a stable stoichiometric chemical structure corresponding to the Si^{4+}(SiO_2) oxidation state. The XPS spectrum of the deep and middle regions results nearly identical as the as-grown case except that it presents a slight reduction in the contribution of the Si^{0+}(Si) oxidation state. The inset in this figure shows the deconvolution of the Si 2*p* peak, which stresses the contribution of the Si^{4+}(SiO_2) oxidation state. The increasing electro-negativity of the Si–O bond relative to the Si–Si bond leads to a shift towards a higher binding energy of the core shell level electrons in the silicon. With regards to the middle graphics corresponding to the SiO*x* film deposited at 100 sccm hydrogen flow level for the case of as-grown film Fig. 5c, similar behavior is observed as that in Fig. 5a. As can be observed, the overlapped curves with a main peak at about 103 eV with a left adjacent shoulder peak at about 100 eV, and the surface region presents two pronounced peaks about 99 eV and 103 eV, attributed to the oxidation state Si^{0+}(Si) and Si^{4+}(SiO_2), respectively, and any other variations could be attributed to the presence of the suboxides.[25,26] Again, the inset in the figure shows the Si 2*p* peaks deconvoluted emphasizing the contribution of the two oxidation states already mentioned. In the Fig. 5d, showing the 100 sccm annealed condition, the XPS Si 2*p* profile presents a variation in the peaks about 99 eV, corresponding to the Si^{0+}(Si) oxidation states, where the deep, middle, and surface curves present a decrease in their intensity peak. The inset in the figure clarifies this through the Si 2*p* peak deconvolution. This situation is contrary to the thermally annealed SiO*x* films deposited at 50 sccm hydrogen flow level, Fig. 5b, where the contributions of the Si^{0+}(Si) oxidation states are absent, and in this case the two peaks remain, Fig. 5c and d, a deconvolution was realized to determine the oxidation states. These results suggest that the hydrogen environment variations have an important influence mainly on the surface regions of the SiO*x* films, as expected since the higher the hydrogen flow level, the higher the concentration of Si and O atoms in the environment is, where such atoms are generated by the etching of the quartz (SiO_2) source

Table II. Compositional results (atomic content, at.%) of the grown SiOx films obtained by XPS composition profiles

		Surface			Middle			Deep		
Flow level		**Si (at.%)**	**O_2 (at.%)**	**C (at.%)**	**Si (at.%)**	**O_2 (at.%)**	**C (at.%)**	**Si (at.%)**	**O_2 (at.%)**	**C (at.%)**
50	As-grown	40.14	55.07	4.78	45.43	53.73	0.83	46.01	53.98	0
100		39.75	53.77	6.46	46.39	53.60	0.63	46.80	53.19	0
50	Annealed	36.4	57.81	6.18	43.74	54.90	0.60	44.10	55.06	0.82
100		37.14	55.62	6.93	44.53	54.77	0.06	44.68	54.31	0.68

affecting the chemical composition of the films. Finally, the bottom graphics, Fig. 5e and f, corresponding to the films grown at a 150 sccm hydrogen flow level exhibit similar qualitative agreement with those of Fig. 5c and d though not accurate qualitatively around the peaks at 99 eV and 100 eV due mainly to the increment of the hydrogen flow level. The XPS composition profiles of the as-grown and thermally annealed SiOx films deposited at 50 sccm and 100 sccm hydrogen flow levels are shown in Fig. 6. This figure is composed of four graphics organized similarly as those in Fig. 5 in relation to the hydrogen flow levels at 50 sccm and 100 sccm; these four graphics represent additional information concerning the chemical elements' atomic percent present in the SiOx films. For this case, the films have a thickness greater than 1 micron, and as can be seen it was not possible to enter into the substrate in these measurements; therefore, it is not possible to get an additional contribution from the substrate, which could be added to our results. The upper-side graphics correspond to the atomic percent for samples grown at 50 sccm hydrogen flow level under the as-grown and annealed conditions. The lower-side graphics correspond to the hydrogen flow level at 100 sccm equally under the as-grown and annealed conditions. From these graphics two common features can be inferred: the first involves the atomic percent variations of the chemical components O1s and Si 2p. It can be seen from these graphics that atomic variations are outstanding only in the approximate range between 0 and 4 at the etch level. The second common feature refers to the uniformity of the atomic percent of the aforementioned chemical constituents, which are present beginning approximately at the 4 etch level. Additionally, another common feature can be found in these graphics, which is related to the atomic percent of the chemical element (carbon) C1s, which decreases only in the approximated range between 0 and 2 at the etch level, and out of this range the C1s is practically reduced to 0 at.%. It is observed from Table II that the major C1s at.% corresponds to the surface region with limits at 4.78% (as-grown) and ~7% (annealed), and it diminishes drastically in the middle and the deep region with a concentration profile $<1\%$. With regards to Si excess, we detect somewhat fluctuating variations in its concentration profile. According to Table II, they are found, when we consider the surface, middle, and deep regions, in such variations we identify the following values: 40.14–46.0% (as-grown, 50 sccm), 39.75–46.80% (as-grown, 100 sccm), 36.4–44.10% (annealed, 50 sccm), and 37.14–44.68% (annealed, 100 sccm). From these data, we can draw two important results: the first is that the Si excess increases mainly in the middle and deep regions of the deposited layer when the hydrogen flow level increases; however, on the surface region, the Si concentration is practically unaffected by the hydrogen flow level changes, although it increases with the increment of the hydrogen flow level only after the thermal treatment. With regard to the oxygen

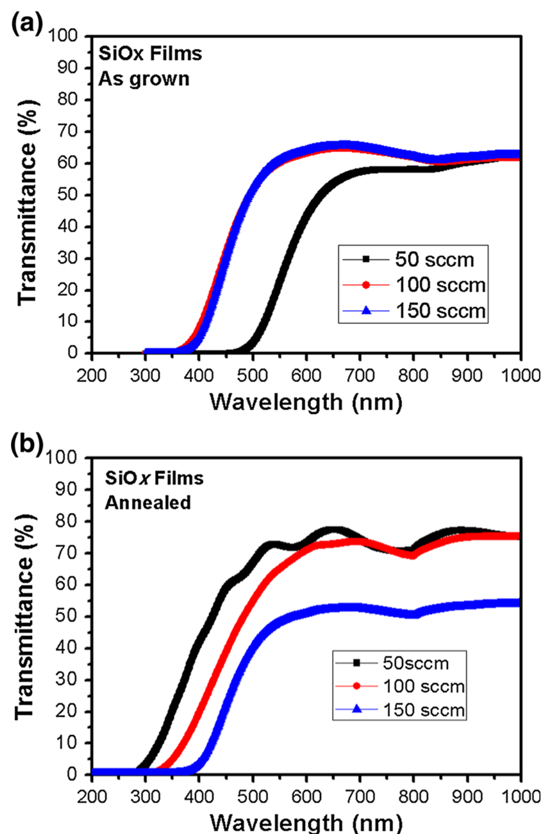

Fig. 7. UV–Vis transmittance spectra as a function of the hydrogen flow levels of the as-grown (a) and annealed (b) SiOx films.

concentration profile, according to the information exhibited in Table II, firstly, we infer that it is reduced with increasing hydrogen flow, which leads to the same quantitative behavior in all regions, but the stoichiometry of the films on the surface region is worth noting in all cases when they were annealed, because (nitrogen) N_2 gas always contains a tiny amount of (oxygen) O_2 impurity which oxidizes Si. Secondly, for the cases of both as-grown and annealed at the 50 sccm hydrogen flow level, the oxygen concentration diminishes in the middle region relative to the surface and finally goes up at the deep region, although with a value less than that at the surface. In addition, for the cases of as-grown and annealed at the 100 sccm hydrogen flow level, the oxygen concentration monotonically decreases starting with its higher value at the surface region. The at.% of each element analyzed within the SiOx films is registered in Table II.

On the other hand, the UV–Vis transmittance spectra of the SiOx films deposited on the quartz substrate at 50 sccm, 100 sccm, and 150 sccm hydrogen flow levels are depicted in Fig. 7. Figure 7a shows two regions of high transmittance corresponding to the as-grown samples. It is identified that the first region corresponds to the curves associated with the hydrogen flow levels at 100 sccm and 150 sccm, which ranges from 350 nm to 1000 nm; in this region, the high transmittance T of both curves lies in the rank of $60\% \leq T \leq 65\%$. For this case neither the transmittance intensities nor optical absorption edges are different in both curves, where their transmittance edge is located about 350 nm, and also, the intrinsic oscillations due to interference effects of radiation in the films are not perceptible as consequence of the film thicknesses which are enough wide that the resonant effects vanish. On the other hand, the second region is located in the range from 350 nm to 1000 nm; in this region the transmittance lies in the rank $55\% \leq T \leq 60\%$ corresponding to the curve associated with the hydrogen flow level at 50 sccm. For this case the transmittance edge is located at ~475 nm. It is noteworthy that both regions of high transmittance converge to the same value of transmittance (~60%). In relation to the thermally annealed samples, Fig. 7b, the first outstanding characteristic is that the overlapped curves are now split each one exhibiting a different absorption edge so we have three different curves. The threshold wavelength for the main transmittance curve (50 sccm) is placed at approximately 275 nm, and this curve reaches the highest transmittance around 75% at 650 nm and 900 nm. Similarly, the transmittance curve corresponding to the hydrogen flow level at 100 sccm has a threshold wavelength around 325 nm and a maximum intensity at ~70%. The third curve, corresponding to the hydrogen flow level at 150 sccm, exhibits a shift in the threshold wavelength towards a longer wavelength of about ~400 nm and a region of strong transmittance that ranges from 550 nm to 1000 nm, with less transmittance (~50%) than that of the 50 sccm and 100 sccm cases. We stress that oscillations due to interference effects of radiation confined inside the film, which had been absent in the case of as-grown condition are now present for the transmittance curve at 50 sccm hydrogen flow level, indicating that the SiOx film has had a reduction in its thickness in such a way that the resonant effects of electromagnetic radiation are now visible as a consequence of dehydrogenation effects. These effects have generated a modification of the atomic structure of the films due to the reduction of the density of Si–H bonds, which in turn must modify the electronic band structure and then the energy band gap (E_g) of the films.[28–30] However, as can be seen, for the transmittance curves associated to the hydrogen flows levels at 100 sccm and 150 sccm this phenomenon about oscillations is not too perceptible because in this case the dehydrogenation process results have little effect on modifying considerably the atomic

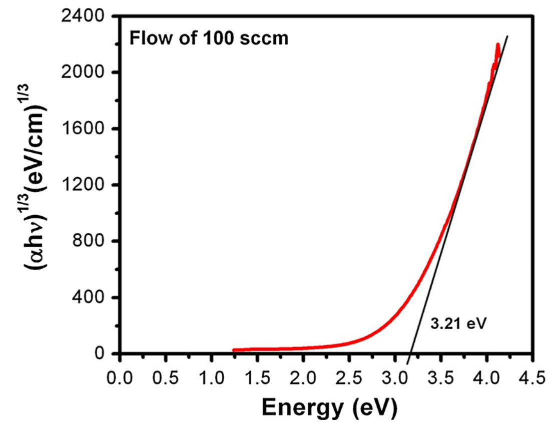

Fig. 8. $(\alpha h\nu)^{1/3}$ versus energy ($h\nu$). Example in order to obtain the E_g approximated value by using the relationship known as Tauc plot of the as-grown film deposited at 100 sccm hydrogen flow level.

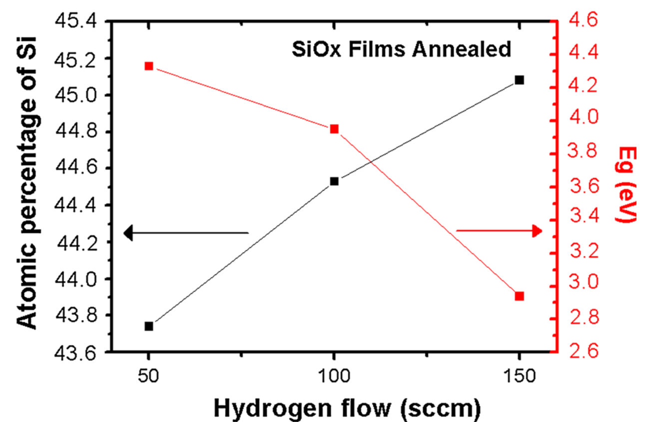

Fig. 9. The E_g (right) and Si atomic concentration variations (left) versus hydrogen flow levels in the thermally annealed SiOx films.

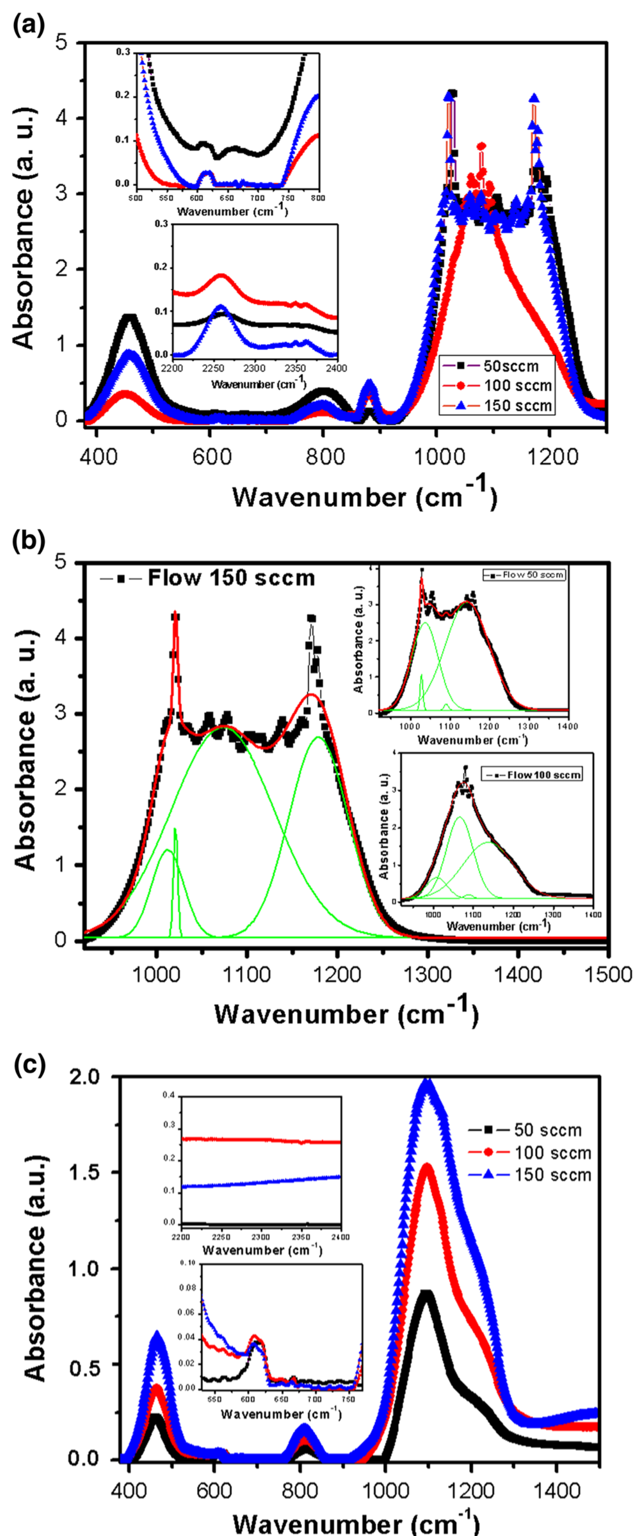

Fig. 10. (a) The FTIR spectra of as-grown SiO*x* films, (b) deconvolution of the as-grown SiO*x* films FTIR spectrum, and (c) FTIR spectra of the thermally annealed SiO*x* films.

composition of the films in such a way that it yields a reduction in the film thickness, despite a decrement in the density of the Si–H bonds. This indicates that dehydrogenation effect induced by the annealing process, which is faster in the film deposited with a lower hydrogen flow level, is a key factor in the optical properties of the films. According to the qualitative and quantitative behavior of the transmittance spectra, it may be concluded that the hydrogen flow level produces, on the one hand, changes in the SiO*x* films' stoichiometry and in their thickness, which produces a shift of the absorption edge, and on the other hand, this same stoichiometric change plays an important role in the energy absorption mechanism due to the presence of Si–H bonds in the material structure. The higher hydrogen flow level produced a greater density of Si–H bonds. When comparing the transmittance spectra of as-grown SiO*x* films with those of the annealed SiO*x* films, it is found that both spectra show an inverse behavior related to their intensities and threshold wavelengths of absorption. By and large, we can asseverate that the variations in the hydrogen flow level generate a wavelength-shift of the absorption edge, which in turn indicates a decrease of the Si excess. For the case of as-grown SiO*x* films, the overall trend seems to be that the lower the hydrogen flow is, the lower transparency of the SiO*x* sample will be, but for the case of the annealed samples the opposite is true. It is remarkable that both as-grown and annealed SiO*x* films are optically active in the visible range. In addition, the notable effect of the thermal annealing process is that it makes easier the formation of absorbing/emitting states (defects or Si-ncs).

In order to know the approximated values of the E_g of the films, we use the relationship known as Tauc plot[29–31] as shown in Fig. 8, where: $\alpha h\nu = A(h\nu - E_g)^n$, E_g is the optical energy bandgap corresponding to a particular band transition in the film; A is a constant and ν the transmission frequency, which determines the photon energy $h\nu$, and the exponent n characterizes the nature of the band transition. The absorption coefficients $\alpha(\lambda)$ were determined from transmission spectra with the following relation: $\alpha(\lambda) = -\ln[T(\lambda)]/d$, where $T(\lambda)$ is the transmittance, and d is the thickness of the SiOx films. α versus $h\nu$ is shown in Fig. 8. On the other hand, values of n = 1/2 and 3/2 correspond to direct allowed and direct-forbidden transitions; n = 2 and 3 are related to indirect-allowed and indirect-forbidden transitions, respectively.[32] From a plot $(\alpha h\nu)^n$ versus $h\nu$, the E_g can be obtained by extrapolating the curve through a straight line, which is prolonged to zero ordinate. The E_g of the as-grown samples shows a random behavior with values at 2.34 eV, 3.16 eV, and 2.87 eV, corresponding to 50 sccm, 100 sccm, and 150 sccm, respectively. However, for the case of the thermal annealed samples, E_g clearly decreases with increasing the hydrogen flow level as it can be seen from Fig. 9. The E_g of the as-grown SiO*x* films lies in the energy range between 3.21 eV and 2.34 eV,

Table III. IR vibration bands[14–19] of the grown SiOx films before and after thermal annealing

Vibration mode	Peak positions (cm^{-1}) As-grown			Annealed		
Flow level (sccm)	50	100	150	50	100	150
Si–O rocking	460	453	457	460	463	469
Si–O bending	800	798	800	819	812	810
Si–O stretching	1024	1008	1020	1095	1097	1091
Si–Si	613	609	611	611	609	609
Si–H wagging	645	650	649	–	–	–
Si–H bending	885	881	881	–	–	–
Si–H stretching	2262	2258	2258	–	–	–

Table IV. Correlation between FTIR and XPS peaks position of the as-grown film deposited at 50 sccm hydrogen flow level

	Bonds and wavenumbers (cm^{-1})		Wavenumber (cm^{-1}) obtained by FTIR	Binding energy (eV) obtained by XPS
1	Si with 2 atoms of O	1020	1027	100.78
2	Si with 3 atoms of O	1060	1037	102.18
3	Si with 4 atoms of O	1120	1089	103.28

whereas that one for the thermally annealed films lies from 4.33 eV to 2.95 eV. When x takes values lower than 2.0 in (amorphous) a SiOx the valence band edge moves up, as the increased Si–Si bond states are gradually overlapped with the oxygen nonbonding states (ONS) and finally spread out into the Si valence band.[32,33] Simultaneously, the conduction band edge also moves down. The final result is that the E_g decreases nonlinearly when Si concentration continually increases.[33] These results agree with the XPS ones, because the Si excess increases with the hydrogen flow level. Overall, the trend for the thermally annealed samples seems to be that the E_g increases when increasing the Si at.% and the Si excess decreases when reducing the hydrogen flow level, as shown in Fig. 9. Therefore, in accordance with the behavior of E_g in Fig. 9, an important conclusion can be drawn which is that the decrement of E_g is strongly dependent on the increment of Si excess which in turn is increased as increasing the hydrogen flow level.

Figure 10 shows the FTIR spectra obtained from the SiOx films. The IR vibration bands are listed in the Table III. All spectra show the absorption characteristic peaks attributed to SiO_2, which correspond to the stretching vibration modes (1082 cm^{-1}), bending (812 cm^{-1}), and rocking (458 cm^{-1}) for Si–O–Si.[4,13–24] Before thermal annealing, these peaks show a shift-wavenumber induced by the hydrogen flow level variations. This suggests a change in the silicon excess, as is shown in Fig. 10a. The stretching vibration mode has a wide peak for SiOx films at 50 sccm flow level, which indicates that different types of Si–O bonds give shape to this peak, as shown in Fig. 10b, and it correlates with the XPS results of the Si 2p for the same SiOx films, as observed in insets of Fig. 5a, b, c, and d. Table IV displays the numerical values of the peak positions of Si–O bonds, obtained from the fitting of the IR stretching band and according to the random bonding model, with which a correlation of both XPS and FTIR characterization techniques can be made. It is clear from Fig. 5a, b, c, and d (lower) that the XPS data reveal the four-oxidation state Si^{n+} (n = 1, 2, 3, 4) and the elemental silicon. Both, XPS and IR exhibit the presence of Si^{2+}, Si^{3+} and Si^{4+}. Indeed, we corroborate the existence of Si–O bonds in the FTIR spectra. From this information it can be deduced that the hydrogen flow level and the growth temperature define the stretching peak. After thermal annealing, the shifts disappear and the position of the vibration modes corresponds to that of SiO_2, thus indicating a phase separation of Si-ncs and SiO_2. The FTIR spectra intensity increases due to the influence of the hydrogen flow level, as observed in Fig. 10c. Additionally, all samples (before and after thermal annealing) exhibit a peak around 609–613 cm^{-1} , which has been associated with Si–Si bonds. Before thermal annealing, a vibration band approximately at 885 cm^{-1}, assigned to Si–H bending and Si–O modes of Si–O–H,[31–33] appeared with a shoulder

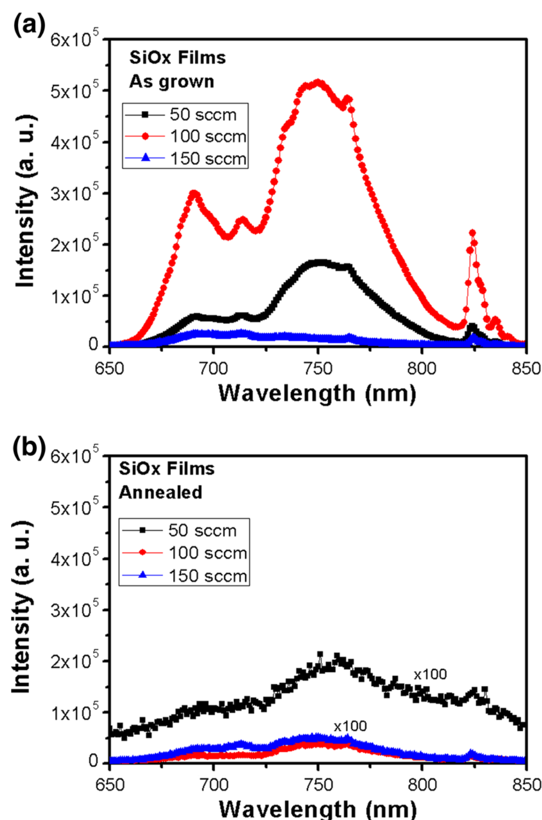

Fig. 11. The PL spectra of as-grown (a) and thermally annealed (b) SiOx films.

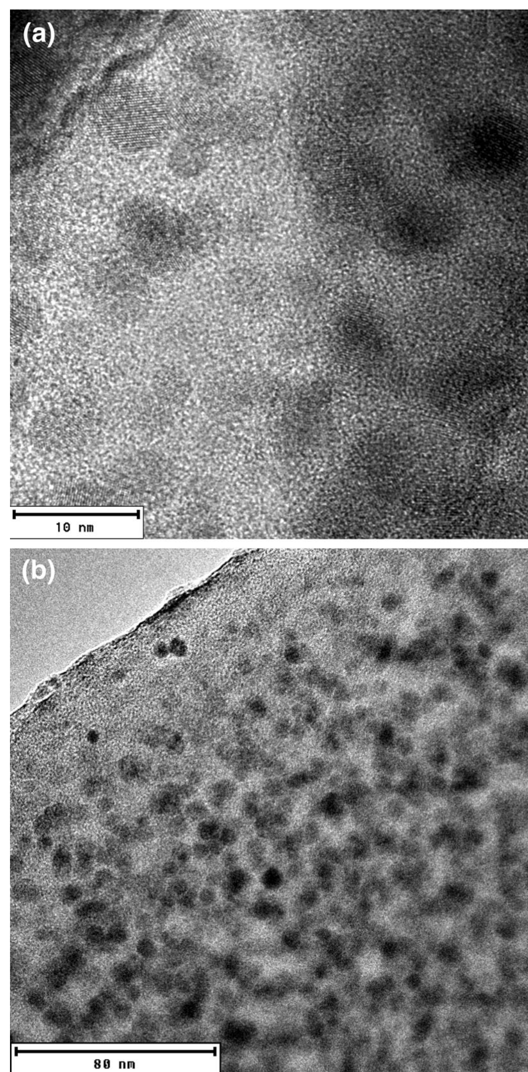

Fig. 12. HRTEM micrograph of a thermally annealed SiOx film, (a) Si nanocrystals, (b) Si-ncs at large scale.

at 810 cm^{-1} related to the Si–O bending vibration mode. On the other hand, with increasing hydrogen flow level, the intensity of the Si–O bending vibration mode decreases and the corresponding peak shifts, at the same time that the peak at 870 cm^{-1} increases, and the Si–O bending vibration band becomes less apparent. These bonds are present in the films due to the incorporation of hydrogen in the experimental process. After the thermal treatment applied to the films, the band at 885 cm^{-1}, disappeared due to hydrogen evaporation at high temperature and the characteristic absorption peaks of SiO_2 were more noticeable. The Si–O stretching vibration band shifted to higher frequencies after thermal annealing indicating a phase separation. Simultaneously, its width is reduced as a result of an increment in the oxygen concentration, as has been revealed by the XPS analysis. Also, before thermal annealing, all samples exhibited not only a peak around 645–664 cm^{-1}, but also around 2258–2262 cm^{-1} as indicated by the insets of Fig. 10a, which in turn are associated with Si–H wagging and Si–H stretching bonds or neutral oxygen vacancies.[34–36] Although the Si–H wagging bonds are practically imperceptible in the main Fig. 10a they are well identified in the upper inset as well as the Si–H stretching bonds are also well identified in the lower inset. The bands associated to these Si–H bonds have disappeared after the thermal annealing due to hydrogen evaporation at high temperature, as is shown in the insets of Fig. 10c.

Figure 11 exhibits the PL spectra of as-grown (a) and thermally annealed (b) SiOx films. From Fig. 11a, corresponding to films under as-grown condition, we can readily see that the major influence of the hydrogen flow level (100 sccm) manifests in the PL spectrum because it possesses not only the greatest intensity, but also the well-defined structure, which has three noticeable peaks. The first peak is placed around 688 nm, the second one around 750 nm, and finally, a third sharp peak around 825 nm. The middle PL spectrum, corresponding to the 50 sccm hydrogen flow level, although noticeably reduced in its intensity, holds a similar shape as the aforementioned first spectrum; however, its peak located around 688 nm has practically vanished. The bottom PL spectrum corresponding to the highest hydrogen flow level is almost collapsed in its intensity although it

maintains a well-defined small peak around 825 nm. A wide PL spectrum is observed for all the samples under as-grown condition. Although the variations induced by the different hydrogen flow levels are well defined in the PL spectra, such variations do not reveal a well-defined tendency. It is clear that such variations modify substantially the appearance of the PL spectra, mainly in their corresponding intensities, which depend strongly on the hydrogen flow, particularly for the case of the hydrogen flow level at 150 sccm where their peaks practically disappear. For this case, keeping in mind that the PL efficiency is the result of the competition between the radiative and the nonradiative recombination process we can deduce that diffusion of the atomic hydrogen into the network of the film not only contributes to the reduction of the nonradiative centers, but also generates defect states in the Si–Si bonds, which act as nonradiative centers overcoming the contribution of the radiative centers to yield a PL quenching. A similar situation is present in the PL spectrum for the hydrogen flow levels (100 sccm and 50 sccm), but for this case the contribution of the radiative centers is stronger in such a way that the PL efficiency is increased. With regard to the thermally annealed SiO*x* films, whose PL spectra are shown in Fig. 11b, two important features are outstanding, the first reveals a drastic reduction in the intensity of the PL spectra, as seen for the hydrogen flow levels at 100 sccm and 150 sccm, whose intensities are the weakest. The second is related to the structure of the PL spectra, which exhibits drastic reductions in the peaks in such a way that the PL curves are practically roughened without outstanding peaks. It is relevant to emphasize that the spectrum shape corresponding to the hydrogen flow level at 50 sccm hardly keeps its original feature after the thermal treatment since it is extinguished and also its intensity becomes weaker. In general, a reduction of the PL intensity in all PL spectra after thermal annealing has been observed, and then we have an important result: the appearance of the PL quenching phenomenon, which is more accentuated for the samples grown at 100 sccm and 150 sccm hydrogen flow levels, offering the weakest PL intensities. In these weak broadened PL spectra, the hydrogen has disappeared, according to the information provided by the FTIR results. Accordingly, this physical situation leads to infer that the atomic hydrogen penetrated into the SiO*x* film and bonded to the Si atom, it passivates the defect states associated with the nonradiative transitions and enhances the PL efficiency, but when it disappears in the films due to the effusion of the atomic hydrogen this fact opens the way to the PL quenching phenomenon in these non-stoichiometric silicon oxide films. At the beginning when these samples are growing the oxygen vacancies are formed with the Si excess, which is being incorporated along with the atomic hydrogen, but later when the annealing process is applied the Si agglomerates displace the vacancies and atomic hydrogen. This behavior is similar to that reported in references,[37–39] where, after annealing, the oxygen interstitials could also change into WOB defects. However, this reaction can be reversed by using excessive thermal annealing energies, which in turn explains the decrease in the PL intensity from WOB defects. Therefore, the thermal annealing produces in the SiO*x* films an increased size of the Si-ncs over the Bohr radius, allowing the quenching of the PL due to the reduction of the size quantum confinement effects associated to the small size of the Si-ncs.

The mechanism of light emission that was considered in the as-grown SiO*x* films, which in turn gives rise to a peak located around 688 nm, is related to a type of defect (NBOHC, NOV, WOB, and E′).[39,40] This defect is one of the principal radiative recombination centers or the luminescence centers produced during the growth process, as has been corroborated in the FTIR spectra. Along with this defect is also the contribution of Si-ncs embedded in SiO*x* whose quantity is augmented by the concentration of silicon excess. This Si concentration was confirmed by means of the XPS profile. Therefore, the light emission from the as-grown SiO*x* films is induced by the combined action of such mechanisms. Apart from this, we identify from such films other PL band placed around 750 nm, which is ascribed to the Si-ncs embedded in the SiO*x* matrix.[24] From the Fig. 11a it is noticeable that the as-grown SiO*x* film deposited at 100 sccm exhibits the highest PL intensity. In relation to the thermal annealing process, it is found that when the thermal annealing is applied to the samples (Fig. 11b), a restructuring occurs (as shown in the FTIR spectra) because the thermal effects cause a phase separation and growth of Si-ncs, as confirmed in Fig. 12a and b, there is clear evidence that at large scales of Si-ncs, and a detailed structural study is on course and will be published elsewhere. Figure 12 shows different Si-ncs with different sizes and crystalline orientations, and also a large amount of Si-ncs was observed in Fig. 12b. When SiO*x* films are submitted to the thermal annealing process, the generated defects in such films are desorbed, thus leading to a decrease in PL intensity. This means that the hydrogen desorption in the samples increments the presence of non-radiative centers. A simple schematic diagram approach of the band structure,[30,41] which attempts to summarize the main energy states localized in the SiO*x* due to the size quantum confinement (Si-ncs) and interfacial states (Si-ncs/Si oxide), is shown in Fig. 13. In this figure, the energy edges of conduction band of bulk Ec(bulk) and valence band of bulk Ev(bulk) determine the bang gap of the silicon, and the ones Ec(NC) and Ev(NC) define the wide band gap of the Si-ncs originated by the quantum confinement, we see that these NC energy edges are deeply localized in the conduction and valence bands of the bulk

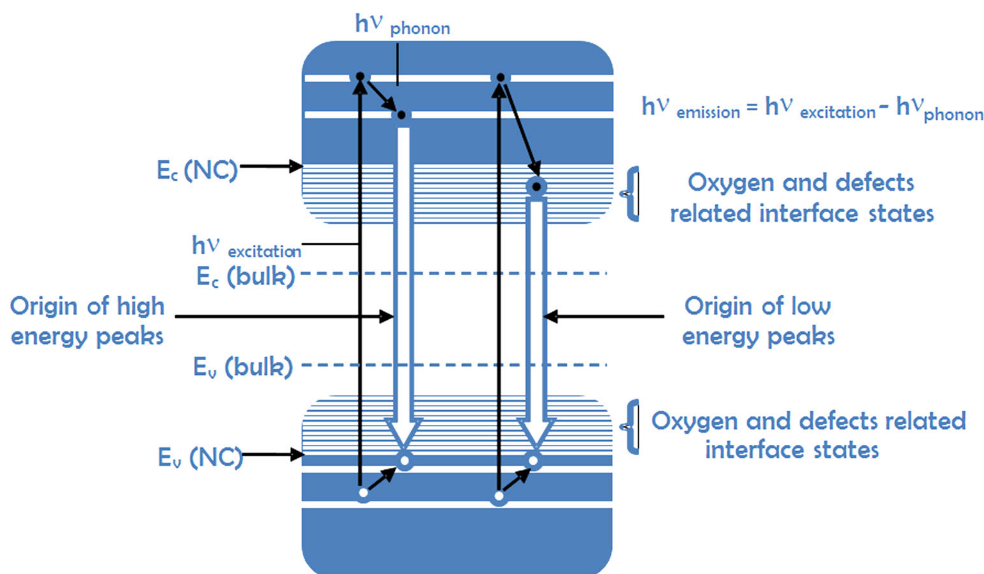

Fig. 13. Schematic of the band structure and PL optical transitions in SiO*x* films with Si-ncs.[41]

material, closely to these edges are situated the remaining energy states coming from interfacial states. Also, in this figure we represent the radiative transitions which produce the emission peaks of the PL and in general we include the nonradiative transitions due to the relax of the hot electrons which originates lattice vibrations (phonons) in the material.

SUMMARY AND CONCLUSIONS

The SiO*x* films deposited by HFCVD technique present noticeable variations in their compositional and optical properties due to both the hydrogen absorption coming from the hydrogen flow and the subsequent annealing effect. The XPS results show a high Si concentration and a low oxygen concentration in the grown SiO*x* films. When the samples were thermally annealed the Si concentration was enhanced as incrementing the hydrogen flow level and the optical energy band gap increased with decreasing the hydrogen flow level. The FTIR results reveal the presence of hydrogen in the as-grown SiO*x* films, whose PL bands are more intense with increasing the hydrogen flow level; however, the hydrogen in Si–H bonds disappears, as confirmed by the same FTIR spectra. Desorption of hydrogen has a significant effect in the PL, because the effusion of hydrogen atoms from the SiO*x* films increments the number of non-radiative centers, which in turn generates the PL quenching. Therefore, it can be concluded that the mechanism of light emission is given by a combined action of the Si-ncs embedded in the SiO*x* films and the defects such as NBOHC. Thus, the films obtained by HFCVD technique exhibit different structural and optical characteristics by the presence and absence of hydrogen atoms in its network. The suitable conditions to deposit SiO*x* films were established in this work, and they have allowed obtaining samples with very good absorption and light emission properties.

ACKNOWLEDGEMENTS

This work has been partially supported by CONACyT-255062 and VIEP-BUAP-LULJ-EXC-2016, PROFOCIE-2016. The authors acknowledge INAOE and IFUAP laboratory for their help in the samples measurements. Authors also want to thank Luis Gerardo Silva from CIMAV-Monterrey for the XPS measurements and University of Texas at San Antonio (UTSA) for the HRTEM measurements.

REFERENCES

1. N.D. Espinosa-Torres, J.A.D. Hernández de la Luz, J.F.J. Flores-Gracia, J.A. Luna-López, J. Martínez-Juárez, and G. Flores Carrasco, *J. Mod. Phys.* 6, 1679 (2015).
2. N.D. Espinosa-Torres, D. Hernández-de la Luz, J.F.J. Flores Gracia, J.A. Luna-López, J. Martínez-Juárez, and D.E. Vázquez-Valerdi, *Nanoscale Res. Lett.* 9, 507 (2014).
3. D. Dong, E.A. Irene, and D.R. Young, *J. Electrochem. Soc.* 125, 819 (1978).
4. Y.C. Fang, W.Q. Li, L.J. Qi, L.Y. Li, Y.Y. Zhao, Z.J. Zhang, and M. Lu, *Nanotechnology* 15, 495 (2004).
5. G.R. Lin, C.J. Lin, and H.C. Kuo, *Appl. Phys. Lett.* 91, 093122 (2007).
6. C.H. Cheng, Y.C. Lien, C.L. Wu, and G.R. Lin, *Opt. Express* 21, 391 (2013).
7. G.G. Sui, X.L. Wu, Y. Gu, and X.M. Boa, *Appl. Phys. Lett.* 74, 1812 (1999).
8. H. Tamura, M. Ruckschloss, T. Wirschem, and S. Veprek, *Appl. Phys. Lett.* 65, 1537 (1994).
9. A.J. Kenyon, P.F. Trwoga, C.W. Pitt, and G.J. Rehm, *Appl. Phys.* 79, 9291 (1996).
10. G.R. Lin, C.J. Lin, C.K. Lin, L.J. Chou, and Y.L. Chueh, *J. Appl. Phys.* 97, 094306 (2005).
11. X.Y. Chen, Y.F. Lu, Y.H. Wu, B.J. Cho, M.H. Liu, D.Y. Dai, and W.D. Song, *J. Appl. Phys.* 93, 6311 (2003).
12. L. Pavesi, L. Dal Negro, L. Mazzoleni, G. Franzo, and F. Priolo, *Nature* 408, 440 (2000).
13. O. Hanaizumi, K. Ono, and Y. Ogawa, *Appl. Phys. Lett.* 82, 538 (2003).

14. K. Kohno, Y. Osaka, F. Toyomura, and H. Katayama, *Jpn. J. Appl. Phys.* 33, 6616 (1994).
15. J.A. Luna López, G.G. Salgado, A.P. Pedraza, D.E.V. Valerdi, J.C. López, A.M. Sánchez, T.D. Becerril, E.R. Andrés, and H.J. Santiesteban, *Procedia Eng.* 25, 304 (2011).
16. P.G. Pai, S.S. Chao, Y. Takagi, and G. Lucovsky, *J. Vac. Sci. Technol. A* 4, 689 (1986).
17. S. Hayashi, S. Tanimoto, and K. Yamamoto, *J. Appl. Phys.* 68, 5300 (1990).
18. L.B. Ma, A.L. Ji, C. Liu, Y.Q. Wang, and Z.X. Cao, *J. Vac. Sci. Technol. B* 22, 2654 (2004).
19. H. Wiesmann, A.K. Ghosh, T. McMahon, and M. Strongin, *J. Appl. Phys.* 50, 3752 (1979).
20. H. Matsumura, *Jpn. J. Appl. Phys.* 37, 3175 (1998).
21. A.H. Mahan, *Thin Solid Films* 395, 12 (2001).
22. S. Nagraj, G.G. Nick, Y. Min-Feng, and S.P. Vanka, *Diam. Relat. Mater.* 17, 79 (2008).
23. F. Piazza, G. Morell, J. Beltran-Huarac, G. Paredes, M. Ahmadi, and M. Guinel, *Carbon* 75, 113 (2014).
24. F. Iacona, G. Franzo, and C. Spinella, *J. Appl. Phys.* 87, 1295 (2000).
25. F. Iacona, C. Borgiono, and C. Spinella, *J. Appl. Phys.* 95, 3723 (2004).
26. L. Wang, K. Han, and M. Tao, *J. Electrochem. Soc.* 154, D91 (2007).
27. J.I. Pankove, *Optical Process in Semiconductors*, 1st ed. (New York: Dover Publications, Inc., 1971), pp. 35–86.
28. L. Pavesi, and R. Turan, *Silicon Nanocrystals: Fundamentals, Synthesis and Applications*, 1st ed. (Weinheim: Wiley-VCH Verlay GmbH & Co KGaA, 2010), pp. 9 and 247.
29. M.S. Valipa, S. Sriraman, E.S. Aydil, and D. Maroudas, *J. Appl. Phys.* 100, 053515 (2006).
30. M. Luppi and S. Ossicini, *Phys. Rev. B* 71, 035340 (2005).
31. F. Gordillo Delgado, J.G. Mendoza Álvarez, and O. Zelaya Ángel, *Rev. Col. de Fís.* 38, 129 (2006).
32. J.A. Luna López, J. Carrillo López, D.E. Vázquez Valerdi, G. García Salgado, T. Díaz Becerril, A. Ponce Pedraza, and F.J. Flores Gracia, *Nanoscale Res. Lett.* 7, 604 (2012).
33. X.Y. Chen, Y. Lu, L.J. Tang, Y.H. Wu, B.J. Cho, J.R. Dong, and W.D. Song, *J. Appl. Phys.* 97, 014913 (2005).
34. F. Ay and A. Aydinly, *Opt. Mater.* 26, 33 (2004).
35. A. Benmessaoud (Doctoral thesis, Universidad Autónoma de Barcelona, Departamento de Física, Bellaterra, 2001), p. 71.
36. F.B. McLean, *IEEE Trans. Nucl. Sci.* 27, 1651 (2001).
37. T. Shimizu-Iwayama, D.E. Hole, and I.W. Boyd, *J. Phys. Condens. Matter* 11, 6595 (1999).
38. T. Morioka, S. Kimura, N. Tsuda, Ch Kaito, Y. Saito, and C. Koike, *Mon. Not. R. Astron. Soc.* 299, 78 (1998).
39. C.-J. Lin and G.-R. Lin, *IEEE J. Quantum Electron.* 41, 441 (2005).
40. G.-R. Lin, C.-J. Lin, and Y. Kuo-Chen, *J. Appl. Phys.* 96, 3025 (2004).
41. M. Ray, S. Minhaz, R.F. Klie, K. Banerjee, and S. Ghosh, *Nanotechnology* 21, 505602 (2010).